



Thermal stability and mechanical properties of arc evaporated Ti–Al–Zr–N hard coatings



S.A. Glatz^{a,b,*}, R. Hollerweger^{a,b}, P. Polcik^c, R. Rachbauer^d, J. Paulitsch^b, P.H. Mayrhofer^{a,b}

^a Christian Doppler Laboratory for Application Oriented Coating Development at the Montanuniversität Leoben, A-8700 Leoben, Austria

^b Institute of Materials Science and Technology, Vienna University of Technology, A-1060 Wien, Austria

^c Plansee Composite Materials GmbH, D-86983 Lechbruck am See, Germany

^d Oerlikon Balzers Coating AG, FL-9496 Balzers, Liechtenstein

ARTICLE INFO

Article history:

Received 15 August 2014

Accepted in revised form 17 January 2015

Available online 24 January 2015

Keywords:

TiAlZrN

PVD

Bias

Phase formation

Oxidation resistance

ABSTRACT

Based on previous reports, showing that zirconium alloying to $Ti_{1-x}Al_xN$ hard coatings can increase their thermal stability, we study in detail the interaction of bias potential and Al content on structure, hardness, thermal stability, and oxidation resistance of arc evaporated $Ti_{1-x-y}Al_xZr_yN$ hard coatings. For moderate Al-contents, $Ti_{0.49}Al_{0.44}Zr_{0.07}N$, their structure is single-phase cubic and their hardness remains at ~35 GPa upon annealing in vacuum to 900 °C, when prepared with –40 and –80 V bias. Contrary, the coatings deposited with –120 V bias experience already for annealing temperatures above 700 °C a hardness reduction from the as deposited value of ~40 GPa. The higher Al-containing $Ti_{0.39}Al_{0.54}Zr_{0.07}N$ coatings are mixed cubic and hexagonal wurtzite type structured, and with increasing bias potential the cubic phase fraction increases. Whereas the coatings prepared with –120 V bias exhibit an almost constant hardness of ~25 GPa upon annealing to 900 °C, their counterparts prepared with lower bias, experience even a slight increase in hardness, due to the formation of well defined crystallites. However, only single-phased cubic structured $Ti_{0.49}Al_{0.44}Zr_{0.07}N$ coatings are able to withstand an oxidation treatment for 20 h in ambient air at 850 °C due to the formation of a dense, protective Al_2O_3 based outer oxide scale. Their oxidation resistance decreases with increasing bias potential, due to the increased defect density and thus promoted diffusion. Based on our studies we can conclude, that although the droplet-size decreases and the as deposited hardness increases with increasing bias potential, their thermal stability and especially oxidation resistance decrease.

© 2015 Elsevier B.V. All rights reserved.

1. Introduction

Hard coatings are designed to meet the requirements for increasing the wear resistance of today's machining applications such as drilling, milling, or cutting. Therefore, in addition to wear resistance also high hardness, oxidation resistance, and thermal stability are necessary [1, 2]. TiN was one of the first industrially applied hard protective coatings. The limited oxidation resistance and hardness were soon further improved by Al-alloying [1–4]. Especially single-phased cubic $Ti_{1-x}Al_xN$ coatings exhibit a pronounced age-hardening effect during annealing to approximately 900 °C and hence this material is also well known for its high mechanical strength even at higher temperatures. This age-hardening effect is based on the spinodal decomposition of the supersaturated $Ti_{1-x}Al_xN$ phase into cubic TiN- and AlN-rich domains. For higher annealing temperatures, the metastable cubic AlN-rich domains (sometimes even c-AlN) further transform into the thermodynamically stable wurtzite (w) AlN modification. However, the hardness

rapidly decreases as soon as pronounced fractions of w-AlN are formed, as w-AlN exhibits an ~26% larger specific volume and lower mechanical strength than c-AlN [5–7].

Therefore, several studies focus on alloying transition metals (TM) to the $Ti_{1-x}Al_xN$ system to form quaternary nitride coatings. The different transition metals can significantly increase the oxidation resistance, thermal stability, as well as mechanical and thermo-mechanical properties [4,8–12].

By now, only little information is available on the influence of Zr addition on the mechanical properties and thermal stability of $Ti_{1-x}Al_xN$ hard coatings [13]. Chen et al. [8,14] and Yang et al. [15] report for magnetron-sputtered $Ti_{0.40}Al_{0.55}Zr_{0.05}N$ and arc evaporated $Ti_{0.45}Al_{0.49}Zr_{0.06}N$, that Zr improves the oxidation resistance of $Ti_{1-x}Al_xN$ hard coatings by promoting the formation of a dense, protective oxide scale. Furthermore, it could be shown that by introducing only small amounts of Zr not only the as deposited hardness values can be increased from ~38 GPa to ~42 GPa but also the decomposition process and hence the age-hardening effect can be shifted to higher annealing temperatures of $T_a = 1000$ °C [8].

Nevertheless, the influence of composition and structure on mechanical properties, thermal stability, and oxidation resistance of arc

* Corresponding author at: Institute of Materials Science and Technology, Vienna University of Technology, Vienna, Austria.

E-mail address: stefan.glatz@tuwien.ac.at (S.A. Glatz).

evaporated $Ti_{1-x-y}Al_xZr_yN$ coatings is still not fully clarified. Therefore, we have prepared arc evaporated $Ti_{1-x-y}Al_xZr_yN$ coatings with different Al contents and using different bias potentials during deposition. These coatings are characterized in detail with respect to their morphology, hardness, thermal stability, and oxidation resistance.

2. Experimental

All $Ti_{1-x-y}Al_xZr_yN$ thin films were deposited by reactive cathodic arc evaporation in an Oerlikon Balzers INNOVA industrial scale deposition plant. Four out of six cathodes were equipped with powder-metallurgically prepared $Ti_{0.475}Al_{0.475}Zr_{0.05}$ or $Ti_{0.375}Al_{0.575}Zr_{0.05}$ targets (Plansee CM GmbH, 99.9% purity, diameter of 160 mm). Silicon (100), polycrystalline alumina (Al_2O_3), austenite platelets, as well as iron foil are used as substrate materials. These substrates were ultrasonically cleaned for 5 min in acetone and in ethanol prior to mounting on the two-fold rotating carousel.

For better adhesion of the coatings, the substrates were ion etched for 25 min in argon atmosphere by using the Balzers INNOVA central beam etching technology. The subsequent 60-minute deposition processes were carried out at a temperature of 500 °C using a nitrogen pressure of 3.5 Pa, and different negative bias potentials of –40, –80, or –120 V.

To eliminate substrate interference, especially during thermal treatments and X-ray diffraction investigations, the coated iron foils were treated in diluted nitric acid (10%) and concentrated hydrochloric acid to dissolve the iron foil. Thereafter, the remaining coating flitters were mechanically grinded in a porcelain mortar to gain $Ti_{1-x-y}Al_xZr_yN$ powder.

For characterizing the crystal structure and phases of the coating materials, X-ray diffraction (XRD) experiments are performed in a Bruker-AXS D8 Advance system in Bragg–Brentano mode with $Cu-K\alpha$ radiation. The crystallite sizes and the internal strains were evaluated by quadratic Williamson–Hall plots.

A HTM Reetz vacuum furnace was used to thermally treat the $Ti_{1-x-y}Al_xZr_yN$ powder and coated Al_2O_3 substrates for 1 h at temperatures ranging from $T_a = 600$ up to 1400 °C. Heating and cooling rates of 30 and 60 K/min, respectively, were used. Oxidation treatments of $Ti_{1-x-y}Al_xZr_yN$ on Al_2O_3 substrates were carried out in a conventional chamber furnace at 850 and 950 °C for 20 h in ambient air atmosphere. The oxidized coatings on Al_2O_3 substrates are protected with a CrN sputter-layer to allow polishing of cross-sections without removing the oxide scales on top. These cross-sections are used for detailed scanning electron microscope (SEM) investigations and energy dispersive X-ray spectroscopy (EDS) line-scans.

A Carl Zeiss Evo 50 SEM was used for investigating the surface and cross-sectional morphology. Chemical analysis was obtained by EDS using the attached Oxford Instruments INCA EDS detector.

The hardness of $Ti_{1-x-y}Al_xZr_yN$ hard coatings on Al_2O_3 substrates was analysed by nanoindentation using a Fischer–Cripps Laboratories Ultra-Micro-Indentation System. This system was equipped with a Berkovich diamond tip and normal loads were reduced from 35 mN to 13 mN in steps of 0.8 mN for each measurement, which resulted in a maximum indentation depth of <10% of the film thickness. The obtained load displacement curves were evaluated after Oliver and Pharr [16].

3. Results and discussion

3.1. As deposited films

Table 1 shows the chemical composition of our stoichiometric $Ti_{1-x-y}Al_xZr_yN$ coatings as a function of the target composition and bias potential used. A comparison of the initial target composition with the metal sublattice composition of the coatings exhibits slightly lower Al/Ti ratios of 47/53 and 58/42 in the coatings as in the used $Ti_{0.475}Al_{0.475}Zr_{0.05}$ and $Ti_{0.375}Al_{0.575}Zr_{0.05}$ targets having Al/Ti ratios of

Table 1
Chemical composition of $Ti_{1-x-y}Al_xZr_yN$ investigated by EDS measurements on austenite substrate.

Target composition				Bias [V]	Film composition							
Al	Ti	Zr	Al/Ti		Absolute				Metal sublattice			
					Al	Ti	Zr	N	Al	Ti	Zr	Al/Ti
[at.%]			Ratio	[at.%]				[at.%]				Ratio
47.5	47.5	5	50/50	–40	21.8	23.9	3.4	50.9	44.4	48.8	6.8	47/53
				–80	21.3	23.9	3.3	51.5	43.9	49.2	6.8	
				–120	21.6	24.1	3.4	50.9	44.0	49.0	7.0	
57.5	37.5	5	60/40	–40	26.1	18.8	3.2	52.0	54.4	39.1	6.6	58/42
				–80	25.7	18.9	3.3	52.1	53.7	39.4	6.9	
				–120	26.0	19.1	3.4	51.5	53.5	39.5	7.0	

50/50 and 60/40, respectively. Moreover, the Zr content increases from 5 at.% in the target to ~7 at.% in the film. We envision that gas scattering and re-evaporation processes (at the substrate surface) are more pronounced for the lighter element Al than for Ti and especially Zr. Compositional variations due to the applied bias potential are within the error of measurement of our EDS analysis. For an easier reading and a better comparability, the nitrogen content of all coatings was normalized to 50 at.% and the slightly different metal compositions due to the bias variation were rounded and averaged. Hence, the coatings deposited from $Ti_{0.475}Al_{0.475}Zr_{0.05}$ and $Ti_{0.375}Al_{0.575}Zr_{0.05}$ targets are labelled as $Ti_{0.49}Al_{0.44}Zr_{0.07}N$ and $Ti_{0.39}Al_{0.54}Zr_{0.07}N$, respectively.

The thickness of $Ti_{0.49}Al_{0.44}Zr_{0.07}N$ coatings almost linearly decreases from 3.19 to 2.65 μm with increasing the bias potential from –40 to –120 V, see Fig. 1. A comparable behaviour is also obtained for the higher Al-containing $Ti_{0.39}Al_{0.54}Zr_{0.07}N$ coatings, showing a thickness reduction from 3.19 to 2.76 μm with an increase in bias potential from –40 to –120 V.

Fracture cross-sectional micrographs of $Ti_{0.49}Al_{0.44}Zr_{0.07}N$ and $Ti_{0.39}Al_{0.54}Zr_{0.07}N$ coated Al_2O_3 substrates exhibit dense and columnar morphologies for all systems investigated, see Fig. 2a–c and Fig. 2d–f, respectively.

With increasing bias potential, the droplet sizes and their number-densities decrease for both coating systems $Ti_{0.49}Al_{0.44}Zr_{0.07}N$ and $Ti_{0.39}Al_{0.54}Zr_{0.07}N$, see their SEM surface images in Fig. 3a–c and Fig. 3d–f, respectively. The increasing energetic bombardment with increasing bias potential causes increasing adatom mobility and also increasing compressive stresses. Thereby the growth and development of droplets, but especially their interference with the growth of the nitride on top of

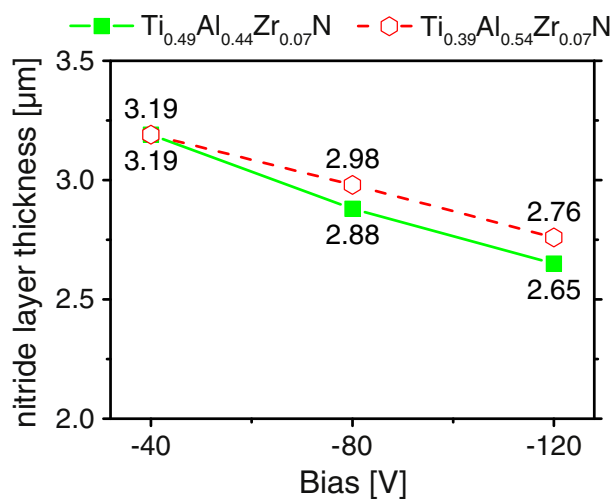


Fig. 1. Thicknesses of $Ti_{0.49}Al_{0.44}Zr_{0.07}N$ and $Ti_{0.39}Al_{0.54}Zr_{0.07}N$ coatings deposited at negative bias potentials of –40, –80, and –120 V in as deposited state on polycrystalline Al_2O_3 substrates.

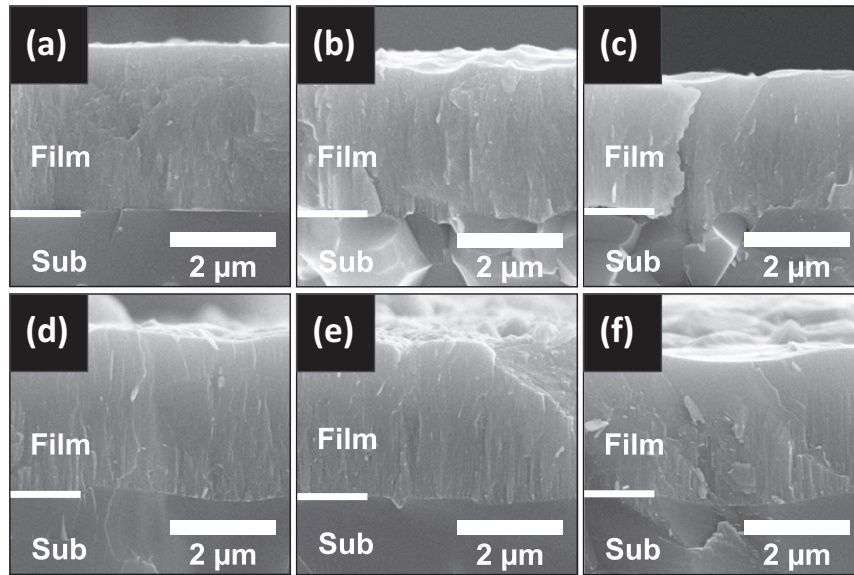


Fig. 2. Fracture cross-sectional SEM micrographs of $\text{Ti}_{0.49}\text{Al}_{0.44}\text{Zr}_{0.07}\text{N}$ (a–c) and $\text{Ti}_{0.39}\text{Al}_{0.54}\text{Zr}_{0.07}\text{N}$ (d–f) coatings deposited at bias potentials of -40 , -80 , and -120 V, respectively.

them are strongly influenced. We envision that with increased adatom mobility, the nucleation and growth of nitride phases on the droplets are promoted leading to a denser and more compact morphology. Thereby, also the overall impression of the surface morphology becomes smoother with increasing bias potential. There is no significant influence of the different Al contents within the targets on the size and amount of generated particles.

XRD patterns of the as deposited $\text{Ti}_{0.49}\text{Al}_{0.44}\text{Zr}_{0.07}\text{N}$ coatings indicate the expected single-phase cubic structure (in comparison with the standard peak positions of cubic TiN [17], cubic AlN [18], and hexagonal AlN [18]), see Fig. 4a. For our Al-rich nitride films ($\text{Ti}_{0.39}\text{Al}_{0.54}\text{Zr}_{0.07}\text{N}$) a significant contribution of an additional phase can be detected, see the increased XRD background between 2θ angles of ~ 30 and ~ 37 deg. in Fig. 4b, which suggests the formation of additional wurtzite and nanocrystalline phases, in agreement with previous reports [19–22]. Mayrhofer et al. [23] showed that the lattice parameters of the hexagonal wurtzite type structured AlN phase decrease with increasing Ti

content. Hence, the XRD peaks at 2θ positions of ~ 32 and ~ 34 deg. suggest the formation of an $\text{Al}_x\text{Ti}_{1-x}\text{N}$ based solid solution next to the cubic $\text{Ti}_{1-x}\text{Al}_x\text{N}$ solid solution. Corresponding observations were also reported in [24–27] by XRD and in [25–27] by TEM and SAED studies. Furthermore, Székely et al. [27] showed the coexistence of c-TiN and w-AlN phases next to the c- $\text{Ti}_{1-x}\text{Al}_x\text{N}$ and the w- $\text{Al}_x\text{Ti}_{1-x}\text{N}$ solid solutions in the as deposited state. The c-TiN and w-AlN phases, having a $\{111\}_{\text{TiN}}110_{\text{TiN}}\{0001\}_{\text{AlN}}11\bar{2}0_{\text{AlN}}$ epitaxial relationship, originate from the decomposition of w- $\text{Al}_x\text{Ti}_{1-x}\text{N}$ solid solution during film growth. With increasing film thickness the texture of the individual phases changes, and in addition to the small grain sizes, various broad overlapping XRD peaks evolve. Thereby, the formation of a broad XRD response at ~ 34 deg. can be explained [27], which is in agreement with the results presented here, see the broader XRD response between ~ 30 and ~ 37 deg. in Fig. 4b. Based on these results, we add the corresponding prefixes c- and c/w- to our coatings to highlight their as deposited structure, c- $\text{Ti}_{0.49}\text{Al}_{0.44}\text{Zr}_{0.07}\text{N}$ and c/w- $\text{Ti}_{0.39}\text{Al}_{0.54}\text{Zr}_{0.07}\text{N}$. For

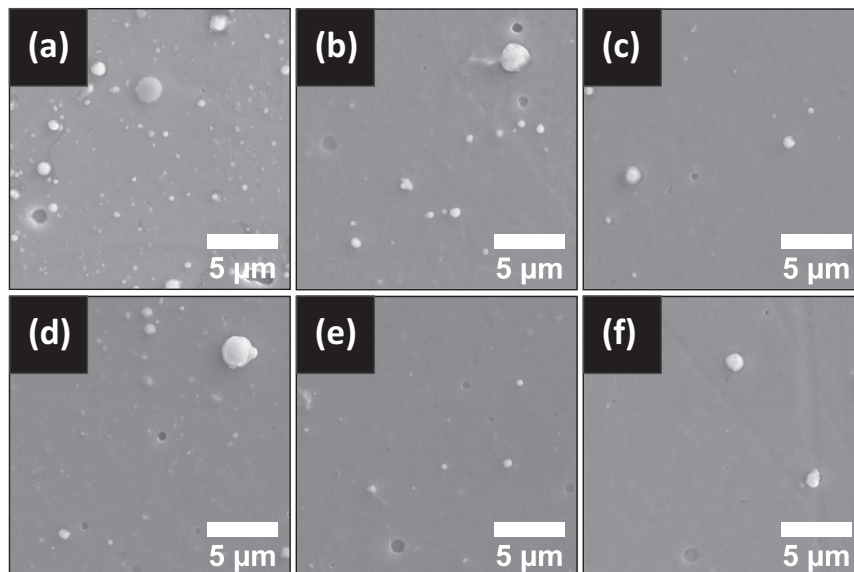


Fig. 3. SEM surface images of $\text{Ti}_{0.49}\text{Al}_{0.44}\text{Zr}_{0.07}\text{N}$ (a–c) and $\text{Ti}_{0.39}\text{Al}_{0.54}\text{Zr}_{0.07}\text{N}$ (d–f) deposited on austenite substrates with bias potentials of -40 , -80 , and -120 V, respectively.

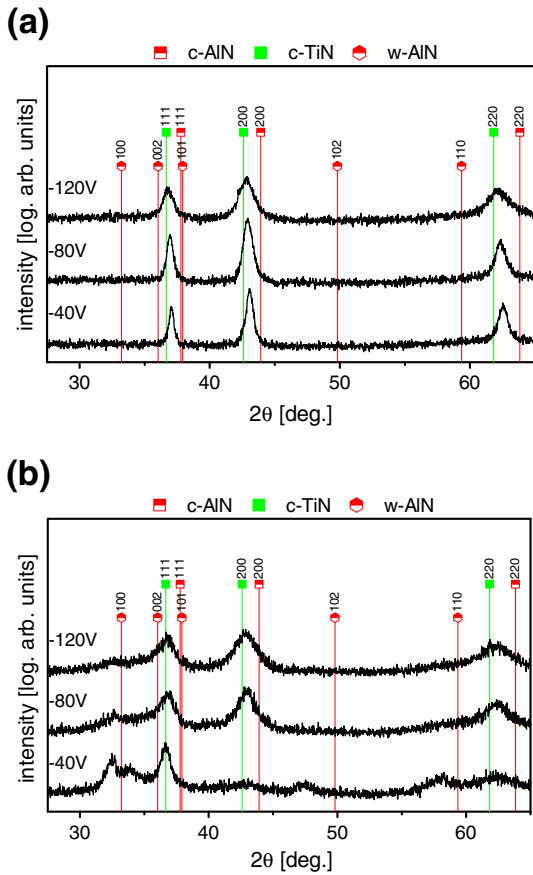


Fig. 4. Powder diffraction patterns of as deposited $\text{Ti}_{0.49}\text{Al}_{0.44}\text{Zr}_{0.07}\text{N}$ (a) and $\text{Ti}_{0.39}\text{Al}_{0.54}\text{Zr}_{0.07}\text{N}$ (b) coatings, prepared with bias potentials of -40 , -80 , and -120 V, respectively.

both coating systems the XRD peaks—from the cubic phase fraction—shift to smaller 2θ angles and become broader with increasing bias potential from -40 to -120 V. For $\text{c-Ti}_{0.49}\text{Al}_{0.44}\text{Zr}_{0.07}\text{N}$, the shift to lower diffraction angles can be attributed to the internal strain, which increases from 0.5 to 1.0% and leads to internal compressive stresses, caused by increasing defect density due to enhancing ion bombardment [7,9]. The latter is also responsible for decreasing crystallite sizes from 24 to 9 nm with increasing bias potential. This is especially visible by the peak broadening of the XRD patterns when increasing the bias potential to -120 V during deposition, see Fig. 4a [28].

Powder diffraction patterns suggest a pronounced dependence of the structure of our Al-rich c/w- $\text{Ti}_{0.39}\text{Al}_{0.54}\text{Zr}_{0.07}\text{N}$ coatings on the bias potential used. The strong wurtzite phase XRD response detected at $2\theta \approx 32$ deg. for coatings deposited with -40 V significantly decreases and the (200) and (220) peaks of the cubic phase increase in intensity with rising bias potential. This clearly shows that with increasing bias potential the formation of the cubic phase is promoted. One major possible explanation for this effect, which is often observed by researchers [29,30], is based on the higher specific density of the cubic phase with respect to the wurtzite phase. Consequently, when the compressive stresses increase, due to increasing energetic bombardment with increasing bias potential, the phase with the higher specific density is favoured. This is in excellent agreement with computational studies, showing that with increasing compressive stresses the cubic phase is preferred over the hexagonal wurtzite type phase [31]. Due to the rather broad and overlapping XRD peaks of the crystalline phases, the determination of their crystallite sizes and internal strains is extremely difficult and gives a huge error bar. However, the Williamson–Hall evaluations suggest crystallite sizes of ~ 4 nm and strains of $\sim 1\%$. Here, the dominant factor for the small crystallite size is mainly based on the competitive dual/multi-phase growth and not on the energy of the impinging particles during growth. In this case, the bias potential has a stronger influence on the phase fractions than on their grain size.

In the as deposited state, our $\text{c-Ti}_{0.49}\text{Al}_{0.44}\text{Zr}_{0.07}\text{N}$ coatings deposited with -40 and -80 V bias potential exhibit hardness values of ~ 35 GPa.

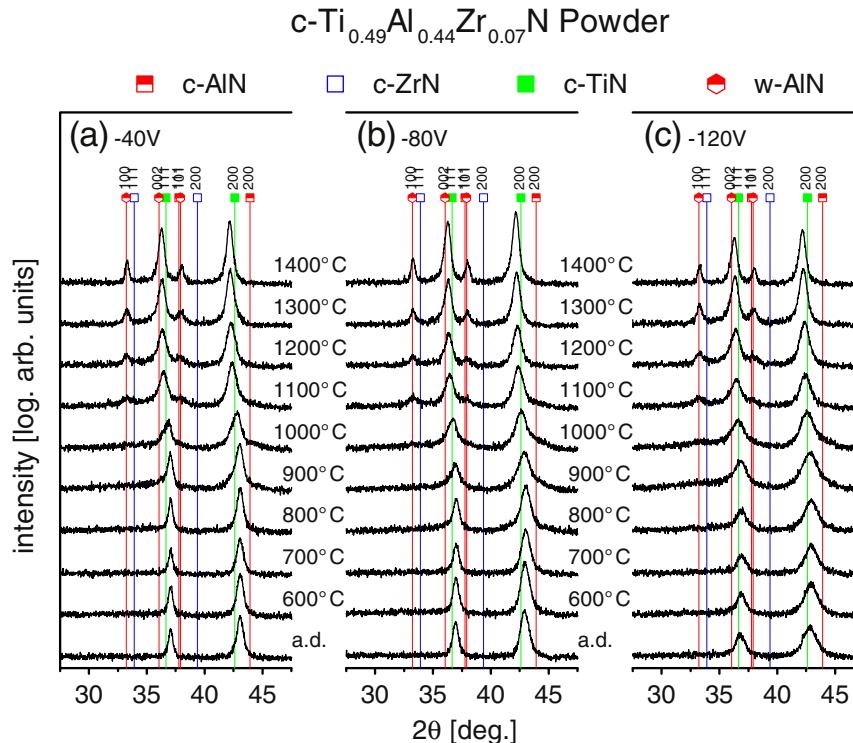


Fig. 5. Powder diffraction patterns of $\text{c-Ti}_{0.49}\text{Al}_{0.44}\text{Zr}_{0.07}\text{N}$ deposited at negative bias potentials of -40 (a), -80 (b), and -120 V (c) in the as deposited (a.d.) state and after vacuum annealing for one hour at $T_a = 600$ to 1400 °C. The standard peak positions of cubic TiN and cubic ZrN, as well as cubic AlN and hexagonal AlN are taken from [17] and [18].

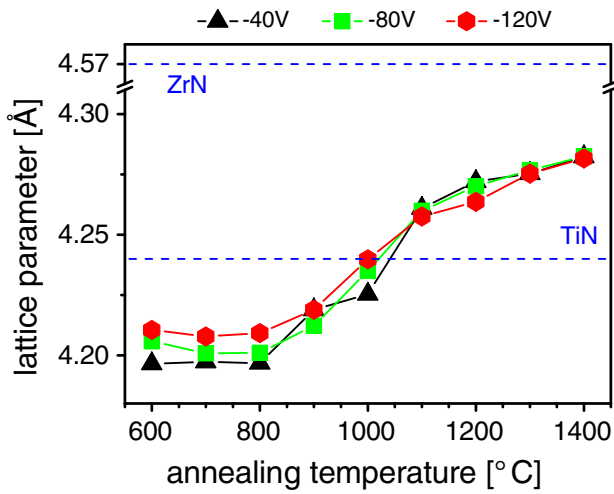


Fig. 6. Development of the lattice parameter for the cubic phase within our $\text{Ti}_{0.49}\text{Al}_{0.44}\text{Zr}_{0.07}\text{N}$ coatings deposited at negative bias potentials of -40 (black triangle), -80 (green square), and -120 V (red hexagon) with increasing annealing temperature T_a from 600 to 1400 °C.

Increasing the bias potential to -120 V significantly enhances the film hardness to around 40 GPa (for further information the reader is referred to Section 3.2). If we compare these hardnesses with the corresponding XRD patterns, Fig. 4a, and the crystallite size and strain evaluation after Williamson–Hall, the increase in hardness is based on grain refinement and increase in compressive stresses. This can clearly be seen by the corresponding diffraction pattern showing that the XRD peaks are much broader and shifted to lower diffraction angles when the coating is prepared with -120 V bias, as compared to the coatings deposited with -40 and -80 V bias. As mentioned above, the variation in chemical composition due to different bias potentials is within the error of

measurement. All $c/w\text{-Ti}_{0.39}\text{Al}_{0.54}\text{Zr}_{0.07}\text{N}$ coatings, which contain significantly higher amounts of Al than $c\text{-Ti}_{0.49}\text{Al}_{0.44}\text{Zr}_{0.07}\text{N}$ coatings exhibit lower hardness values, due to the presence of wurtzite phases. This can clearly be seen when comparing Fig. 4b with Fig. 4a, showing the presence of XRD peaks at the position for the wurtzite phase for our $c/w\text{-Ti}_{0.39}\text{Al}_{0.54}\text{Zr}_{0.07}\text{N}$ coatings. The obtained increase in hardness from ~ 19 to ~ 25 GPa with increasing bias potential up to -120 V is mainly based on the concomitant increase in their cubic phase fractions—see the XRD patterns in Fig. 4b. Cubic structured $\text{Ti}_{1-x}\text{Al}_x\text{N}$ coatings are generally much harder and stiffer than their wurtzite structured counterparts [5,7,15,28,32–34].

3.2. Thermal stability

With increasing annealing temperatures T_a , the cubic XRD peaks of our single-phase cubic structured $c\text{-Ti}_{0.49}\text{Al}_{0.44}\text{Zr}_{0.07}\text{N}$ coatings shift to lower 2θ values for $T_a \geq 900$ °C, which indicates an Al-depletion from the supersaturated $\text{Ti}_{1-x-y}\text{Al}_x\text{Zr}_y\text{N}$ solid solution. This is valid for all bias potentials used, see Fig. 5a, b, and c, which show the XRD patterns taken after various annealing treatments of our coatings prepared with -40 , -80 , and -120 V, respectively. After annealing at $T_a = 900$ °C, the first indications of a shoulder formation on the right side of the (200) peak can be detected, especially visible for the coating prepared with -80 V (Fig. 5b). This shoulder formation suggests the formation of Al-enriched cubic domains and is an indication for spinodal decomposition of the supersaturated cubic-phase $\text{Ti}_{1-x}\text{Al}_x\text{N}$ based matrix into cubic Al-rich and Ti-rich domains [5,8,35,36]. The formation of Ti-rich cubic domains is difficult to detect for our coatings, as the XRD peaks of the cubic-phase $\text{Ti}_{1-x}\text{Al}_x\text{N}$ matrix are very close to the $c\text{-TiN}$ position, especially for $T_a = 900$ and 1000 °C. Upon further increase in annealing temperature, the cubic Al-rich domains transform into wurtzite AlN and further increase in the wurtzite AlN phase fraction occurs, see the (100) XRD peak of the $w\text{-AlN}$ phase at $2\theta \approx 33$ deg. After annealing at 1400 °C the coatings are completely decomposed into $w\text{-AlN}$ and a cubic TiN-rich phase. As no additional $c\text{-ZrN}$ phase can be

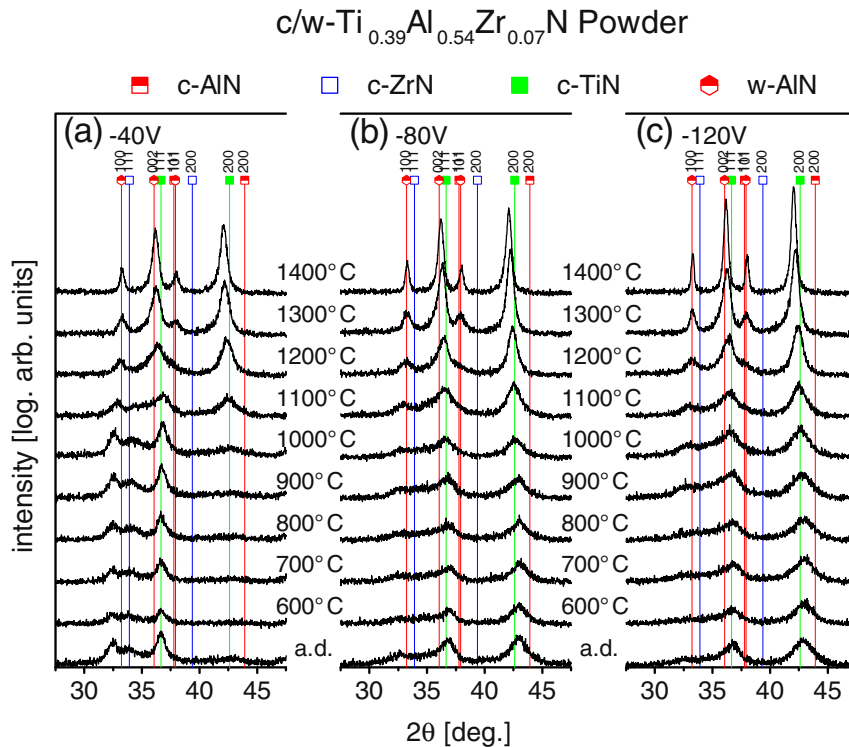


Fig. 7. Powder diffraction patterns of $c/w\text{-Ti}_{0.39}\text{Al}_{0.54}\text{Zr}_{0.07}\text{N}$ deposited at negative bias potentials of -40 (a), -80 (b), and -120 V (c) in the as deposited (a.d.) state and after vacuum annealing for 1 h at $T_a = 600$ to 1400 °C.

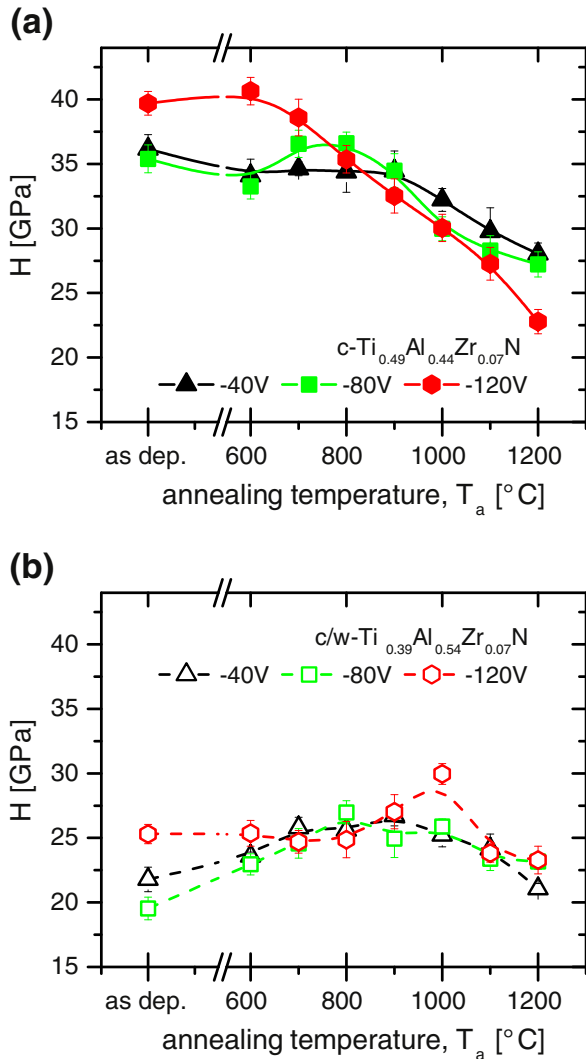


Fig. 8. Hardness values for $c\text{-Ti}_{0.49}\text{Al}_{0.44}\text{Zr}_{0.07}\text{N}$ (a) and $c/w\text{-Ti}_{0.39}\text{Al}_{0.54}\text{Zr}_{0.07}\text{N}$ (b) coatings after vacuum annealing for 1 h at T_a up to 1200 °C.

detected and the XRD peaks of the $c\text{-TiN}$ -rich phases are located at the left side of the $c\text{-TiN}$ standard peak positions, we suggest that a solid solution $c\text{-Ti}_{1-x}\text{Zr}_x\text{N}$ is formed. This is in agreement with phase diagrams and further experiments showing a huge solubility for ZrN in TiN, and vice versa, especially at elevated temperatures [13,37,38]. The composition of $\text{Ti}_{1-x}\text{Zr}_x\text{N}$ can be calculated after $z = y / (1 - x)$ with y and x from $\text{Ti}_{1-x}\text{Al}_x\text{Zr}_y\text{N}$. Hence, for our $c\text{-Ti}_{0.49}\text{Al}_{0.44}\text{Zr}_{0.07}\text{N}$ coatings a $c\text{-Ti}_{0.88}\text{Zr}_{0.12}\text{N}$ phase will form. Moreover, for this maximum annealing temperature, the XRD peaks become sharper suggesting grain growth.

The development of the lattice parameter for the cubic phase, with increasing annealing temperature, within our coatings, Fig. 6, clearly shows increasing values with $T_a \geq 900$ °C. Independent of the bias potential used during deposition, the lattice parameters approach 4.282 Å with $T_a = 1400$ °C. This value is in excellent agreement with 4.28 Å reported for $\text{Ti}_{0.89}\text{Zr}_{0.11}\text{N}$ [8], and 4.28 Å for $\text{Ti}_{0.88}\text{Zr}_{0.12}\text{N}$ from a linear interpolation between 4.24 Å for TiN [17] and 4.57 Å for ZrN [17] (i.e., $0.88 \cdot 4.24 \text{ \AA} + 0.12 \cdot 4.57 \text{ \AA} = 4.28 \text{ \AA}$).

The higher Al-containing $c/w\text{-Ti}_{0.39}\text{Al}_{0.54}\text{Zr}_{0.07}\text{N}$ coatings exhibit already in the as deposited state a multi-phase structure, composed of nanocrystalline wurtzite and cubic phases, Fig. 4b. Annealing of the coatings prepared with -40 V bias, see Fig. 7a, leads to a shift of the (100) XRD peak of the wurtzite solid solution towards the position for $w\text{-AlN}$. Simultaneously, the (200) peak of the cubic phase develops. This can especially be seen for $T_a \geq 1000$ °C. Further annealing of this sample to 1400 °C results in a completed decomposition and relaxation, with the formation of $w\text{-AlN}$ and a $c\text{-Ti}_{0.85}\text{Zr}_{0.15}\text{N}$ solid solution (if all the zirconium is solved in this phase). This corresponds to the results obtained for the lower Al-containing coatings.

$\text{Ti}_{0.39}\text{Al}_{0.54}\text{Zr}_{0.07}\text{N}$ coatings deposited at -80 V (Fig. 7b) and -120 V (Fig. 7c), which have also a pronounced cubic phase fraction (in addition to the wurtzite phase) already in the as deposited state, exhibit for $T_a \approx 1000$ °C a decomposition behaviour of the cubic phase similar to that of $c\text{-Ti}_{0.49}\text{Al}_{0.44}\text{Zr}_{0.07}\text{N}$, compare Fig. 5. However, comparing the XRD patterns of $c\text{-Ti}_{0.49}\text{Al}_{0.44}\text{Zr}_{0.07}\text{N}$ and $c/w\text{-Ti}_{0.39}\text{Al}_{0.54}\text{Zr}_{0.07}\text{N}$ obtained after annealing at $T_a = 1400$ °C, Figs. 5 and 7, respectively, shows that sharper diffraction peaks are obtained for $c/w\text{-Ti}_{0.39}\text{Al}_{0.54}\text{Zr}_{0.07}\text{N}$. Nevertheless, the dual/multi-phase nature of $c/w\text{-Ti}_{0.39}\text{Al}_{0.54}\text{Zr}_{0.07}\text{N}$ thin films enables them to be very resistant against structural changes upon annealing at lower temperatures. Up to $T_a = 1100$ °C, no significant changes in the XRD patterns for our Al-rich $c/w\text{-Ti}_{0.39}\text{Al}_{0.54}\text{Zr}_{0.07}\text{N}$ coatings can be observed. We envision, that this is mainly based on the nanocrystalline

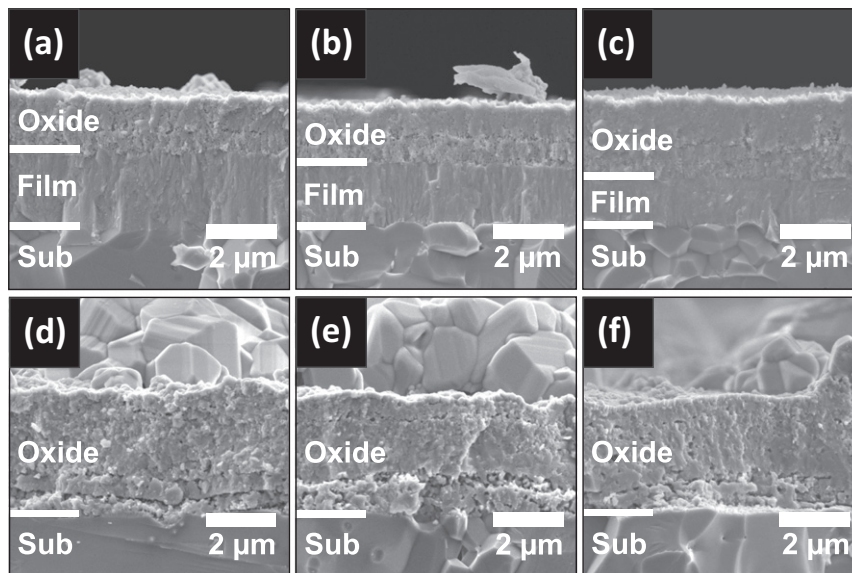


Fig. 9. Fracture cross-sectional micrographs of $c\text{-Ti}_{0.49}\text{Al}_{0.44}\text{Zr}_{0.07}\text{N}$ coatings deposited with -40 , -80 , and -120 V bias after 20 h of oxidation at 850 (a, b, c) and 950 °C (d, e, f), respectively.

nature of the coatings. As soon as a pronounced crystalline XRD peaks can be detected, as for $T_a = 1100\text{ }^\circ\text{C}$, the overall structure starts pronounced grain growth and decomposition processes, see Fig. 7a–c. On the other hand, although the single-phase cubic $c\text{-Ti}_{0.49}\text{Al}_{0.44}\text{Zr}_{0.07}\text{N}$ coatings exhibit a detectable structural change already for annealing temperatures below $1100\text{ }^\circ\text{C}$, see Fig. 5a–c, the more homogeneous distribution of w-AlN—as they originate from a decomposition of the supersaturated cubic phase—guarantee for a retarded grain growth at higher temperatures.

Hardness measurements of $c\text{-Ti}_{0.49}\text{Al}_{0.44}\text{Zr}_{0.07}\text{N}$ coatings prepared at -40 V bias reveal stable hardness values of around 35 GPa up to $T_a = 900\text{ }^\circ\text{C}$, see Fig. 8a. This is also the temperature where a shoulder-formation at both sides of the (111) and (200) XRD peaks (Fig. 5a) and hence the formation of Al-depleted and Al-rich cubic domains due to spinodal decomposition can be observed. Higher annealing temperatures result in a decrease of the hardness to $\sim 28\text{ GPa}$ at $T_a = 1200\text{ }^\circ\text{C}$ due to the formation and growth of w-AlN precipitates. A similar hardness evolution over temperature can be observed for the $c\text{-Ti}_{0.49}\text{Al}_{0.44}\text{Zr}_{0.07}\text{N}$ coatings prepared with -80 V of bias. The coatings prepared with -120 V exhibit already higher as deposited values of $\sim 40\text{ GPa}$ which can be maintained up to $T_a = 700\text{ }^\circ\text{C}$. Upon further annealing, the hardness then decreases to $\sim 23\text{ GPa}$ at $T_a = 1200\text{ }^\circ\text{C}$. Such a steep decrease in hardness (especially for $T_a \geq 900\text{ }^\circ\text{C}$) together with highest hardness in as deposited state, might be attributed to the smaller grain size and higher defect density of the coatings prepared with -120 V bias. Therefore, diffusion and hence decomposition is promoted. The thermal stability of materials decreases with increasing defect density and decreasing grain size [7,36, 39–41].

Contrary to the single-phase cubic coatings, the mixed cubic/wurtzite structured $c/w\text{-Ti}_{0.39}\text{Al}_{0.54}\text{Zr}_{0.07}\text{N}$ coatings, see Fig. 8b, show increasing hardness values up to annealing temperatures of $1000\text{ }^\circ\text{C}$, which decreases again upon further increasing T_a . As already discussed for the as deposited state, the mechanical properties of these coatings mainly depend on the cubic phase fractions. Hence, the coatings prepared with -120 V bias, exhibiting larger cubic phase fraction, also have higher hardness values than those prepared with lower bias potentials. Nevertheless, their hardness is below that of single-phase cubic $c\text{-Ti}_{0.49}\text{Al}_{0.44}\text{Zr}_{0.07}\text{N}$. Due to coating delamination, hardness measurements could not be conducted on samples annealed at temperatures above $1200\text{ }^\circ\text{C}$.

3.3. Oxidation behaviour

The oxidation behaviour is investigated only for single-phase cubic $c\text{-Ti}_{0.49}\text{Al}_{0.44}\text{Zr}_{0.07}\text{N}$ coatings, as due to the multi-phase structure of the Al-rich coatings a lower oxidation resistance is obtained, and the

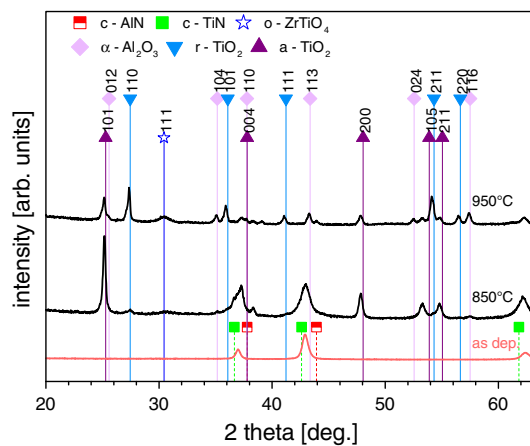


Fig. 10. Powder diffraction patterns of $\text{Ti}_{0.49}\text{Al}_{0.44}\text{Zr}_{0.07}\text{N}$ prepared with bias potentials of -80 V before and after 5 h of oxidation at 850 and $950\text{ }^\circ\text{C}$.

coatings were already fully oxidized after 20 h exposure to air at $850\text{ }^\circ\text{C}$. Corresponding results have been published for Zr-free $\text{Ti}_{1-x}\text{Al}_x\text{N}$ coatings as a function of their Al content and structure [5]. Cross-sectional SEM images of our coatings after 20 h oxidation at 850 and $950\text{ }^\circ\text{C}$ in ambient air are presented in Fig. 9a–c and Fig. 9d–f, respectively. All single-phase $c\text{-Ti}_{0.49}\text{Al}_{0.44}\text{Zr}_{0.07}\text{N}$ coatings, oxidized at $850\text{ }^\circ\text{C}$, exhibit an oxide scale that is able to protect the nitride layer underneath.

XRD studies of free standing coating materials, after oxidation in ambient air at 850 and $950\text{ }^\circ\text{C}$ for 5 h, Fig. 10, clearly show that for $850\text{ }^\circ\text{C}$ the major oxide phase is anatase [42]. This is in agreement with earlier studies [14], showing that Zr promotes the anatase formation. With increasing temperature the fraction of the rutile phase [42] strongly increases on the expense of the anatase phase and also crystalline $\alpha\text{-Al}_2\text{O}_3$ [43] and ZrTiO_4 [43] based oxides can be detected.

EDS line-scans across the coating and oxide scale, Fig. 11a, clearly show the remaining nitride layer without detectable oxygen content at the coating-substrate interface region, when the oxidation temperature is $850\text{ }^\circ\text{C}$. An oxide scale, clearly exhibiting two different regions, follows this nitrogen rich area. At the interface to the nitride layer, a Ti-enriched and Al-depleted oxide scale is formed which is followed by an Al-enriched and Ti-depleted oxide scale at the outer most surface

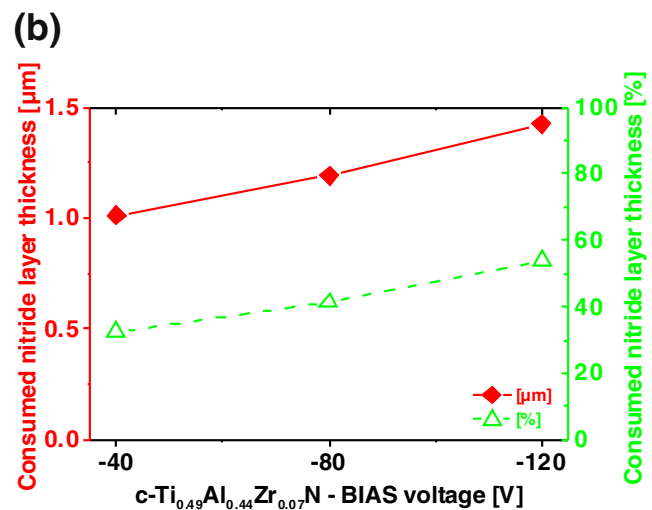
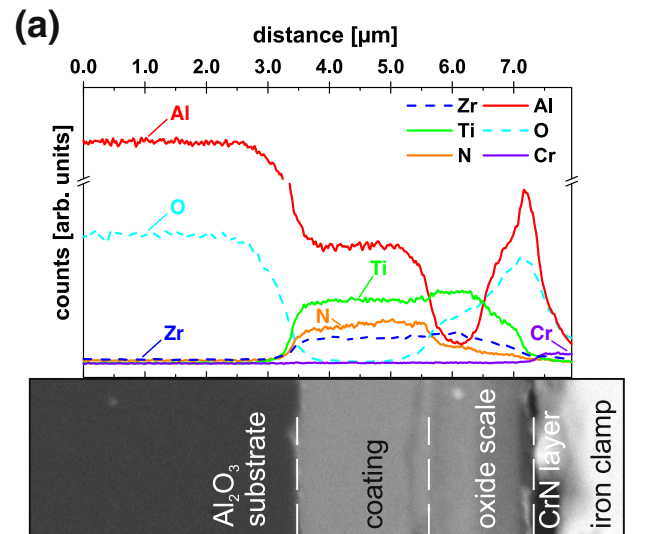


Fig. 11. EDS line-scans and backscattered electron SEM images of the polished cross-section of $c\text{-Ti}_{0.49}\text{Al}_{0.44}\text{Zr}_{0.07}\text{N}$ deposited with -80 V bias after 20 h of oxidation at $850\text{ }^\circ\text{C}$ (a). Consumed nitride layer thickness of $c\text{-Ti}_{0.49}\text{Al}_{0.44}\text{Zr}_{0.07}\text{N}$ coatings after 20 h of oxidation at $850\text{ }^\circ\text{C}$ as a function of applied bias potential (b).

to the ambient air. Moreover, the Al signal clearly indicates a layered structure of alternating Al-rich and Al-depleted areas. These phase separations within the oxide scale are commonly observed for $Ti_{1-x}Al_xN$ based coating systems and depend on the different affinity of Ti and Al to oxygen, their outward diffusion rates, and the inward diffusion rate of O [5,8,10,11,44,45]. Zirconium shows a similar compositional variation across the sample as Ti, with a slight increasing content directly above the nitride layer, indicating that a mixed Ti–Zr-oxide is formed. Our results are in agreement to previous reports showing that for $Ti_{0.40}Al_{0.55}Zr_{0.05}N$ coatings a $Ti_{0.67}Zr_{0.33}O_2$ and Al_2O_3 oxide is formed [8,14].

The comparison of the layer thickness of $c-Ti_{0.49}Al_{0.44}Zr_{0.07}N$ in the as deposited state and after oxidation shows that more than 60% of the original coating thickness remains. However, with increasing bias potential from -40 to -120 V, the consumed nitride layer thickness increases significantly, see Fig. 11b. The enhanced oxide scale growth and the accompanied reduction in nitride layer thickness with increasing bias are based on the higher defect densities and smaller grain size of the coatings prepared with higher bias potential. Thereby, diffusion processes are considerably enhanced leading to a promoted oxide scale growth.

After isothermal annealing in ambient air at 950 °C for 20 h the coatings are fully oxidized, see Fig. 9d–f, which show the cross-sections of coatings prepared with -40 , -80 , and -120 V, respectively. The fully oxidized state is also represented by the corresponding EDS line-scans. Fig. 12 shows an example of the fully oxidized coating, prepared with -120 V, after oxidation in ambient air at 950 °C for 20 h. The corresponding EDS line-scans clearly show the compositional fluctuations especially for Ti and Al across the entire oxide scale. In general, the outer region is rich in Al, and the inner region—which is near the substrate and hence the latest oxidized area—is rich in Ti. But the line-profile clearly shows smaller fluctuations, where Ti-rich areas alter with Al-rich areas. Such a layered structure can be based on the fact that the increasing stresses—accompanied with increasing thicknesses of Al-based and Ti-based oxide scales—can lead to cracking of the protective and dense Al_2O_3 outer most layer. Thereby, further oxidation is promoted due to open pathways for oxygen to the unprotected nitride and the formation of a layered Al-based and Ti-based oxide scale starts again [46,47]. Noteworthy is, that the intensity increase of the Ti signal on top of the oxide scale, hence even after the Al-peak (Fig. 12), stems from the formation of extremely large Ti-based oxide grains. These are clearly visible in the corresponding SEM cross-sections, Fig. 9d–f.

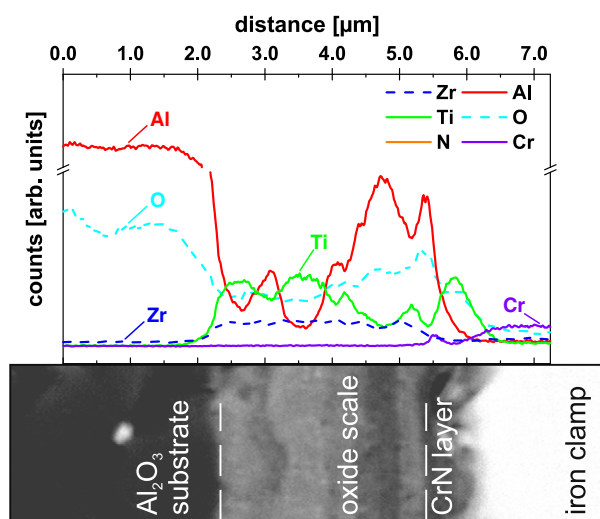


Fig. 12. EDS line-scans and backscattered electron SEM images of the polished cross-section of $c-Ti_{0.49}Al_{0.44}Zr_{0.07}N$ deposited with -120 V bias after 20 h of oxidation at 950 °C.

4. Summary and conclusions

We have investigated the influence of substrate bias potential and chemical composition on structural development, mechanical and thermal stability, as well as oxidation resistance of cathodic arc evaporated single-phase cubic $c-Ti_{0.49}Al_{0.44}Zr_{0.07}N$ and mixed cubic/wurtzite structured $c/w-Ti_{0.39}Al_{0.54}Zr_{0.07}N$ hard coatings. With increasing bias potential from -40 to -120 V we have observed decreasing film thickness, decreasing grain sizes and increasing defect density—suggested by XRD investigations—for single-phase $c-Ti_{0.49}Al_{0.44}Zr_{0.07}N$ coatings. Thereby, also the hardness increases from ~ 35 to ~ 40 GPa. The higher Al-containing $c/w-Ti_{0.39}Al_{0.54}Zr_{0.07}N$ thin films exhibit increasing cubic phase fraction and enhanced hardness with increasing bias potential from -40 to -120 V. During vacuum annealing treatments up to about 900 °C, $c-Ti_{0.49}Al_{0.44}Zr_{0.07}N$ thin films can maintain their as deposited hardness values of ~ 35 GPa, as the formation of new Al-depleted and Al-rich cubic domains—formed via spinodal decomposition process—actively act as obstacles against plastic deformation. With increasing annealing temperatures T_a , the Al-rich cubic domains phase transform to the thermodynamically stable wurtzite structured $w-AlN$ and also grain coarsening can be observed. The combination of these processes leads to decreasing hardness values to ~ 28 GPa at $T_a = 1200$ °C. The $c-Ti_{0.49}Al_{0.44}Zr_{0.07}N$ coating prepared with -120 V bias exhibits the highest as deposited hardness of ~ 40 GPa, which can be maintained up to an T_a of 700 °C. But for $T_a \geq 900$ °C their hardness values are below that of their lower bias counterparts. The multiple phase containing $c/w-Ti_{0.39}Al_{0.54}Zr_{0.07}N$ coatings show generally lower hardness values. Whereas up to 1000 °C even a hardness increase and above that temperature a decreasing hardness due to promoted $w-AlN$ formation and grain growth can be obtained. Although our $c-Ti_{0.49}Al_{0.44}Zr_{0.07}N$ coatings have a lower Al content than $c/w-Ti_{0.39}Al_{0.54}Zr_{0.07}N$, their oxidation resistance is superior due to their single-phase cubic structure. Even after a 20 h exposure in air at 850 °C only a thin oxide scale—with a Ti- and Zr-rich area towards the nitride and an Al-enriched outermost region—forms on top of the coating, which effectively protects the nitride layer underneath against further oxidation. Increasing the bias potential up to -120 V leads to promoted oxidation, as the thereby increased defect densities within the coatings promote diffusion. Oxidation treatments for 20 h at 950 °C lead to a complete consumption of the nitride coatings.

Based on our findings we can conclude, that for high thermal stability and oxidation resistance low defect density within the coatings is important. Especially, for our multi-phased $Ti_{1-x-y}Al_xZr_yN$ coatings the higher Al content cannot even compensate the thereby reduced thermal stability. Consequently, our arc evaporated single-phase cubic $c-Ti_{0.49}Al_{0.44}Zr_{0.07}N$ coatings outperform their higher Al-containing but multi-phased counterparts in mechanical strength, thermal stability, and oxidation resistance.

Acknowledgements

The financial support by the Austrian Federal Ministry of Economy, Family and Youth and the National Foundation for Research, Technology and Development is greatly acknowledged. We also thank for the financial support of Plansee Composite Materials GmbH and Oerlikon Balzers Coating AG.

References

- [1] F.-R. Weber, F. Fontaine, M. Scheib, W. Bock, Surf. Coat. Technol. 177–178 (2004) 227–232.
- [2] H. Prengel, P. Jindal, K. Wendt, A. Santhanam, P. Hegde, R. Penich, Surf. Coat. Technol. 139 (2001) 25–34.
- [3] W.-D. Münz, J. Vac. Sci. Technol. A Vac. Surf. Film 4 (1986) 2717–2725.
- [4] I.J. Smith, W.D. Münz, L.A. Donohue, I. Petrov, J.E. Greene, Surf. Eng. 14 (1998) 37–42.
- [5] L. Chen, J. Paulitsch, Y. Du, P.H. Mayrhofer, Surf. Coat. Technol. 206 (2011) 2954–2960.

- [6] A. Hörling, L. Hultman, M. Oden, J. Sjolen, L. Karlsson, *Surf. Coat. Technol.* 191 (2005) 384–392.
- [7] P.H. Mayrhofer, C. Mitterer, L. Hultman, H. Clemens, *Prog. Mater. Sci.* 51 (2006) 1032–1114.
- [8] L. Chen, D. Holec, Y. Du, P.H. Mayrhofer, *Thin Solid Films* 519 (2011) 5503–5510.
- [9] M. Pfeiler, K. Kutschej, M. Penoy, C. Michotte, C. Mitterer, M. Kathrein, *Surf. Coat. Technol.* 202 (2007) 1050–1054.
- [10] R. Rachbauer, D. Holec, P.H. Mayrhofer, *Surf. Coat. Technol.* 211 (2012) 98–103.
- [11] M. Pfeiler, C. Scheu, H. Hutter, J. Schnöller, C. Michotte, C. Mitterer, et al., *J. Vac. Sci. Technol. A Vac. Surf. Film* 27 (2009) 554.
- [12] R. Rachbauer, D. Holec, M. Lattemann, L. Hultman, P.H. Mayrhofer, *Int. J. Mater. Res.* 102 (2011) 735–742.
- [13] O. Knotek, M. Böhmer, T. Leyendecker, F. Jungblut, *Mater. Sci. Eng. A* 105–106 (1988) 481–488.
- [14] L. Chen, L. He, Y. Xu, L. Zhou, F. Pei, Y. Du, *Surf. Coat. Technol.* 244 (2014) 87–91.
- [15] B. Yang, L. Chen, Y.X. Xu, Y.B. Peng, J.C. Fen, Y. Du, et al., *Int. J. Refract. Met. Hard Mater.* 38 (2013) 81–86.
- [16] W.C. Oliver, G.M. Pharr, *J. Mater. Res.* 19 (2004) 3–20.
- [17] International Center for Diffraction Data, PDF-4/Release, 2010.
- [18] International Center for Diffraction Data, PDF-4/Release, 2010.
- [19] I.A. Saladukhin, G. Abadias, A. Michel, S.V. Zlotski, V.V. Uglov, G.N. Tolmachova, et al., *Thin Solid Films* 538 (2013) 32–41.
- [20] J. Martan, P. Beneš, *Thermochim. Acta* 539 (2012) 51–55.
- [21] D. Holec, R. Rachbauer, L. Chen, L. Wang, D. Luef, P.H. Mayrhofer, *Surf. Coat. Technol.* 206 (2011) 1698–1704.
- [22] R. Rachbauer, S. Massl, E. Stergar, D. Holec, D. Kiener, J. Keckes, et al., *J. Appl. Phys.* 110 (2011) 023515.
- [23] P.H. Mayrhofer, D. Music, J.M. Schneider, *J. Appl. Phys.* 100 (2006) 094906.
- [24] L. Chen, *Thin Solid Films* 517 (2009) 6635–6641.
- [25] M. Moser, P.H. Mayrhofer, *Scr. Mater.* 57 (2007) 357–360.
- [26] M. Moser, P.H. Mayrhofer, L. Székely, G. Sáfrán, P.B. Barna, *Surf. Coat. Technol.* 203 (2008) 148–155.
- [27] L. Székely, G. Sáfrán, V. Kis, Z.E. Horváth, P.H. Mayrhofer, M. Moser, et al., *Surf. Coat. Technol.* 257 (2014) 3–14.
- [28] C. Wüstefeld, D. Rafaja, V. Klemm, C. Michotte, M. Kathrein, *Surf. Coat. Technol.* 205 (2010) 1345–1349.
- [29] R. Franz, M. Lechthaler, C. Polzer, C. Mitterer, *Surf. Coat. Technol.* 206 (2012) 2337–2345.
- [30] R. Franz, M. Lechthaler, C. Polzer, C. Mitterer, *Surf. Coat. Technol.* 204 (2010) 2447–2453.
- [31] D. Holec, F. Rovere, P.H. Mayrhofer, P.B. Barna, *Scr. Mater.* 62 (2010) 349–352.
- [32] K. Kutschej, P.H. Mayrhofer, M. Kathrein, P. Polcik, R. Tessadri, C. Mitterer, *Surf. Coat. Technol.* 200 (2005) 2358–2365.
- [33] G. Greczynski, J. Lu, J. Jensen, I. Petrov, J.E. Greene, S. Bolz, et al., *Thin Solid Films* 556 (2014) 87–98.
- [34] P.H. Mayrhofer, F.D. Fischer, H.J. Böhm, C. Mitterer, J.M. Schneider, *Acta Mater.* 55 (2007) 1441–1446.
- [35] M. Bartosik, R. Daniel, Z. Zhang, M. Deluca, W. Ecker, M. Stefanelli, et al., *Surf. Coat. Technol.* 206 (2012) 4502–4510.
- [36] P.H. Mayrhofer, C. Mitterer, H. Clemens, *Adv. Eng. Mater.* 7 (2005) 1071–1082.
- [37] R.A. Andrievskii, I.A. Anisimova, *Inorg. Mater.* 27 (1991) 1220–1223.
- [38] P. Duwez, F. Odell, *J. Electrochem. Soc.* 97 (1950) 299.
- [39] L. Hultman, *Vacuum* 57 (2000) 1–30.
- [40] G. Gottstein, *Physikalische Grundlagen der Materialkunde*, Springer Berlin Heidelberg, Berlin, Heidelberg, 2007.
- [41] H.-J. Bargel, G. Schulze, *Werkstoffkunde*, 11th ed. Springer Berlin Heidelberg, Berlin, Heidelberg, 2012.
- [42] International Center for Diffraction Data, PDF-4/Release, 2010.
- [43] International Center for Diffraction Data, PDF-4/Release, 2010.
- [44] R. Rachbauer, A. Blutmager, D. Holec, P.H. Mayrhofer, *Surf. Coat. Technol.* 206 (2012) 2667–2672.
- [45] F. Vaz, L. Rebouta, M. Andritschky, M.F. Da Silva, J.C. Soares, *J. Eur. Ceram. Soc.* 17 (1997) 1971–1977.
- [46] F. Rovere, R. Braun, J.M. Schneider, P.H. Mayrhofer, *MRS Fall Meet.*, Boston, 2008.
- [47] P. Panjan, B. Navinšek, A. Cvelbar, A. Zalar, I. Milošev, *Thin Solid Films* 281–282 (1996) 298–301.